

1 **A NEW LAGRANGIAN BASED SHORT TERM PREDICTION**
2 **METHODOLOGY FOR HF RADAR CURRENTS**

3
4 Lohitzune Solabarrieta^{1,2}, Ismael Hernandez-Carrasco³, Anna Rubio², Michael Campbell¹, Ganix
5 Esnaola^{4,5}, Julien Mader², Burton H. Jones¹, Alejandro Orfila³

6 (1) KAUST, Red Sea Research Center, Integrated Ocean Processes, Saudi Arabia.

7 (2) AZTI Marine Research, Basque Research and Technology Alliance (BRTA), Pasaia, Spain

8 (3) Instituto Mediterráneo de Estudios Avanzados. IMEDEA (CSIC-UIB), 07190 Esporles,
9 Spain.

10 (4) Nuclear Engineering and Fluid Mechanics Dept., UPV ,20018-Donostia, Spain.

11 (5) Joint Research Unit BEGIK, (IEO)- (UPV/EHU), 48620-Plentzia, Spain.

12 Corresponding author's email: lsolabarrieta@azti.es

13
14 **ABSTRACT**

15 The use of High Frequency Radar (HFR) data is increasing worldwide for different
16 applications in the field of operational oceanography and data assimilation, as it
17 provides real-time coastal surface currents at high temporal and spatial resolution.
18 In this work, a Lagrangian based empirical real-time, Short-Term Prediction (L-
19 STP) system is presented in order to provide short term forecasts of up to 48 hours
20 of ocean currents. The method is based on finding historical analogues of
21 Lagrangian trajectories obtained from HFR surface currents. Then, assuming that
22 the present state will follow the same temporal evolution as the historical analogue
23 did, we perform the forecast. The method is applied to two HFR systems covering
24 two areas with different dynamical characteristics: the southeast Bay of Biscay and
25 the central Red Sea. A comparison of the L-STP methodology with predictions
26 based on persistence and reference fields are performed in order to quantify the
27 error introduced by this approach. Furthermore, a sensitivity analysis has been
28 addressed to determine the limit of applicability of the methodology regarding the
29 temporal horizon of Lagrangian prediction. A real-time skill-score has been
30 developed using the results of this analysis, which allows to identify periods when
31 the short-term prediction performance is more likely to be low, and persistence can
32 be used as a better predictor for the future currents.

36 The coastal zone is under increasing human pressure. During recent decades
37 coastal seas have been experiencing intensified activity for recreation, transport,
38 fisheries and marine-related energy production, which, in many cases, results in
39 serious damage to coastal marine ecosystems. A better understanding of the
40 dynamical processes responsible for the surface oceanic transport is a prerequisite
41 for the efficient management of the coastal ocean. Coastal processes are
42 responsible for the transport and fate of multi-source pollutants like plastics,
43 nutrients, jellyfish, harmful algal blooms, etc. Thus, improving the capacity of
44 monitoring and forecasting the coastal area is key for the integrated assessment of
45 the marine ecosystem. This requirement is driving the set-up of a growing number
46 of multi-platform operational observatories designed for continuous monitoring of
47 the coastal ocean from international or national (e.g., US IOOS, EU EOOS,
48 Australian IMOS, etc.) to local scales. Moreover, due to the need of forecasting
49 applications for response to emergency situations such as oil spills, or search and
50 rescue operations, many of the existing operational observatories are linked with
51 operational ocean forecasting models with or without data assimilation (e.g.
52 MARACOOS, NOAA Global Real-Time Ocean Forecast System, COPERNICUS
53 Marine Environment Monitoring System).

54 With the need of providing a long-term framework for the development and
55 improvement of the European Marine coastal observations, the JERICO Research
56 Infrastructure (JERICO-RI) has been developing methods and tools (through
57 JERICO, JERICO-NEXT and JERICO-S3 projects) for the production of high-
58 quality marine data, and sharing expertise and infrastructures between the existing
59 observatories in Europe. Typically constituted with different in-situ point-wise
60 observational platforms (such as moored buoys, tidal gauges, drifting buoys, etc.) a
61 significant number of these observatories now employ land-based High Frequency
62 Radars (HFR) that provide real-time coastal currents with unprecedented coverage
63 and resolution (e.g. Paduan and Rosenfeld, 1996; Kohut and Glenn, 2003; Abascal
64 et al., 2009; Solabarrieta et al., 2014, Rubio et al. 2017; Paduan and Washburn,
65 2013). Each HFR coastal site measures radial surface currents moving away or
66 approaching the antenna, based on the shift of the first peak (Bragg peak) of the
67 Doppler spectra (Crombie 1955, Barrick et al 1977). Combining the overlapping
68 radial vectors from at least 2 antennas provides surface true vector currents
69 (Barrick et al., 1977, Barrick and Lipa, 1979). Several studies have compared *in-*
70 *situ* current measurements with HFR observations (e.g., Schott et al. 1985;
71 Hammond et al. 1987; Paduan and Rosenfeld 1996, Emery et al. 2004; Paduan et
72 al., 2006; Ohlmann et al. 2007; Liu et al., 2014; Solabarrieta et al, 2014, Bellomo

73 et al., 2015; Lana et al., 2016; Hernandez-Carrasco et al., 2018b) and have
74 repeatedly demonstrated the potential of this technology. Presently, more than 250
75 HFR antennas are installed and active worldwide (Roarty et al., 2019; [http://global-
hfradar.org/](http://global-
76 hfradar.org/)).

77 Due to their high spatio-temporal resolution, HFR data are commonly used in real
78 time for search and rescue (Ullman et al., 2006) or oil spill prediction/mitigation
79 emergency response (Abascal et al., 2017). In addition, there have been several
80 efforts dedicated to the development of assimilation strategies that incorporate the
81 HFR measured surface currents into ocean coastal models (Breivik and Saetra,
82 2001, Oke et al 2002, Paduan and Shulman 2004, Stanev et al., 2011, Barth et al.,
83 2011), some of which have been tested for short periods of time (Chao et al.,
84 2009). However, assimilation of HFR data into models is still a computationally
85 expensive and complex issue, not to mention operational capabilities of such a
86 procedure. Because of these constraints, the availability of real-time high-
87 resolution HFR current fields has led to alternative solutions in order to obtain
88 short term prediction (STP) of surface coastal currents, through the direct use of
89 HFR historical and nowcast observations using different approaches (e.g. Zelenke
90 2005, Frolov et al. 2012, Barrick et al., 2012, Orfila et al. 2015, Solabarrieta et al.
91 2016, Vilibić et al, 2016, Ren et al., 2019, see Table 1).

92 The above-mentioned studies develop and implement different STP approaches
93 (harmonic analysis of the last hours, genetic algorithms, numerical models, ...)
94 which often require either additional data, or long training periods of data without
95 gaps. Hardware failures due to power issues, communications or environmental
96 conditions often result in spatio-temporal gaps within HFR datasets. Spatial gaps
97 can be filled on a real-time basis but filling long temporal gaps is not
98 straightforward. Several gap-filling methodologies have been developed for HFR
99 data sets: Open Modal Analysis, (OMA) (Kaplan and Lekien, 2007), Data
100 Interpolating EOFs (DINEOF) (Hernandez-Carrasco et al., 2018), and Self-
101 Organizing Maps (SOM) (Hernandez-Carrasco et al., 2018).

102 Given the motivation described above, and developed partially within the
103 framework of JERICO-NEXT project, we present a Lagrangian-based Short-Term
104 Prediction (L-STP from now on) methodology using existing HFR datasets, to be
105 applied to surface current real-time observations. The proposed L-STP
106 methodology aims to be capable to use the previously developed gap filling OMA
107 method and generate forecasts in near-real time with low computational costs,
108 compared to the previously presented forecast methods, but with the same level of
109 assessment. The uniqueness of this approach is two-fold: first, the historical

110 Eulerian velocity fields are used to construct a catalogue of Lagrangian trajectories
111 and second, using the trajectories obtained from present observations, analogues in
112 the past dataset are searched in order to obtain the best predictive match. The
113 method is based on Lagrangian computations which have proven to be robust
114 against errors in velocity field data and against the dynamics of unresolved scales,
115 since the averaging effect produced by integrating over trajectories which extend in
116 time and space, tends to cancel random-like errors (Hernandez-Carrasco et al.,
117 2011, Sayol et al., 2014). Consequently, they are reliable for the assessment of the
118 dynamical flow structures.

119 Analogues is a widely used method in time series prediction, especially in early
120 weather forecasting and statistical downscaling. It is based on the assumption that
121 if the behavior of a dynamical system at a given time is similar or close enough to
122 some other situation in the historical record, then the evolution in the future of the
123 state of the system will be similar to the evolution observed in the same historical
124 record. Simply stated, two analogue fields are two distinct fields that are close
125 enough considering a given metric, to be considered as equivalent. Finding of the
126 best (nearest) analogue of a specific time does not require a historically continuous
127 dataset, as long as the dataset contains subsets of observations that extend longer
128 than the testing period and are representative of the range of potential states that
129 the system can have. These statistically analogue events occur naturally in the
130 environment and this methodology has been applied and tested in atmospheric
131 forecasts (Lorenz, 1969, Jianping et al,1993, Prince and Goswami 2007, Shao and
132 Li 2013).

133 It must be stressed that this is the first time that the analogues technique has been
134 applied to the HFR-derived ocean surface currents to obtain short-term forecast, to
135 the knowledge of the authors. The L-STP is intended to be implemented
136 operationally with low computational cost (seconds to few minutes for each
137 forecast, depending on the size of the historical dataset) and is easily implemented
138 using existing HFR data processing tools.

139 **2. DATA AND METHODS**

140 *2.1 Data*

141 HFR data from two distinct oceanographic regions have been used for the
142 evaluation, validation, and testing of the developed methodology (Figure 1): The
143 Bay of Biscay (hereinafter BoB HFR) and the central Red Sea region (hereinafter
144 Red Sea HFR). The range and the spatial resolution of the HFR current systems
145 depend on their working frequency and the conductivity of the water over which
146 the system is measuring. Ranges vary from 15 to 220 km range and spatial

147 resolution from 250 m to 12 km. Typically, a 12 MHz radar has a range ~70 km
148 with a spatial resolution of 2-5 km. HFR systems usually average current
149 measurements for one hour, although some average currents for shorter periods,
150 such as 30 minutes. HFR data from these two regions are used to evaluate the skill
151 of the method under different dynamical conditions, and with a sufficient set of
152 observations to provide a database suited to the efficient research of appropriate
153 analogues. The BoB HFR system, located in the southeastern corner of the Bay of
154 Biscay, in the Basque Country, is composed of two CODAR Seasonde sites,
155 working since 2009 at 4.5 MHz frequency, covering up to 200 km range and
156 providing hourly surface velocity field at 5 km of spatial resolution. The dataset
157 used in this study spans the period from January 2012 to December 2015. The Red
158 Sea HFR system is located on the central western coast of Saudi Arabia and is also
159 composed of two CODAR Seasonde sites. The Red Sea sites are operational since
160 June 2017, transmit at 16.12MHz frequency, covering up to 120 km range and
161 providing the hourly surface velocity field at 3 km spatial resolution. The dataset
162 used in this study spans the period from June 2017 to October 2018.

163 The BoB HFR has been chosen as the pilot system for testing the developed
164 methodology, since it has the longest data series and because several papers have
165 already provided an extensive description of the local circulation and dynamical
166 processes (Rubio et al., 2013a, 2013b, 2018, 2019, 2020; Solabarrieta et al 2014,
167 Solabarrieta et al., 2015, Hernandez-Carrasco et al. 2018, Manso-Narvarte et al.,
168 2018; Declerk et al., 2019). The resulting methodology is then applied to the
169 operational Red Sea HFR dataset, as a study case. Coastal dynamics in the BoB
170 show a clear seasonality where cyclonic and anticyclonic eddies dominate in
171 winter and summer, respectively in responding to local winds and the mean coastal
172 current (Iberian Poleward Current) (Esnaola et al., 2013, Solabarrieta et al., 2014).
173 The circulation in the central Red Sea also demonstrates a clear seasonality
174 (Sofianos and Johns, 2003; Yao et al., 2014a, 2014b; Zarokanellos et al., 2017a,
175 2017b) linked to the seasonal winds of the area (Abualnaja et al., 2015; Langodan
176 et al., 2017b). The region is dominated by eddy activity, with both cyclonic and
177 anticyclonic eddies occurring in the region (Zhan et al., 2014; Zarokanellos et al.
178 2017a). Due to the only recently available dataset (since mid-June 2017 to present)
179 the detailed small-scale surface circulation processes of this area is under
180 characterization at the moment.

181 The primary difference between the two HFR systems is the operating frequency
182 resulting in a larger spatial coverage for the BoB HFR than for the Red Sea HFR
183 and a higher spatial resolution for the latter (5km and 3 km, respectively). This
184 difference in the spatial resolution should result in better capturing the small-scale

185 dynamical features in the Red Sea, which could influence the selection of an
186 analogue.

187 The data from both systems have been processed similarly. The spectra of the
188 received backscattered signal are converted into radial velocities using the
189 MULTiple SIGNAL Classification (MUSIC) algorithm (Schmidt 1986). HFR Progs
190 MATLAB package (<https://github.com/rowg/hfrprogs>) is then used to combine
191 radial currents and generate gap-filled total 2D currents, by means of the Open
192 Modal Analysis (OMA) methodology of Kaplan and Lekien (2007).

193 *2.2 Lagrangian analogues*

194 The proposed prediction system, based on the analogue identification method, has
195 been developed with the objective of providing HFR velocity fields forecast (up to
196 48 hours). As an innovative element, we use a Lagrangian approach in searching
197 for analogues through an historical library composed of particle trajectories,
198 instead of the commonly used Eulerian velocity fields. In our methodology we find
199 the best analogue by comparing maps of trajectories obtained from the last
200 available 48 hours (target field) with the historical catalogue of maps of
201 Lagrangian trajectories (hereinafter Lagrangian catalogue). Then the catalogue
202 map with the trajectory pattern closest to the target field map is selected. Relying
203 on the similar evolution of the current situation and the past analogue, the next 48-
204 hour time velocity fields of the selected analogue provides the target period
205 forecast. In other words, if we find a state in the historical database that is “close
206 enough” to the target field, we assume that the forecast for the current observations
207 will evolve in the same way as did for the chosen analogue. A detailed description
208 of the short-term prediction system is provided in the following algorithm:

- 209 1. *Lagrangian catalogue configuration*. First, to build the Lagrangian
210 catalogue, a set of synthetic trajectories was computed by advecting N
211 particles uniformly initialized on a regular grid (Figure 2) in the OMA HFR
212 velocity fields. The N Lagrangian particles are released every hour over the
213 whole available velocity data and are advected during 48 hours. The maps
214 of trajectories of the catalogue are referred as to \mathbf{X}_C .
- 215 2. *Target map*. A map of trajectories corresponding to the most recent HF
216 currents observations, and referred as to \mathbf{X}_T , is computed using the same
217 procedure than for the Lagrangian catalogue but now advecting the N
218 particles in the available last 48 hours (t_f-48h) of HFR velocity fields, where
219 t_f corresponds to the current time.

220 3. *Searching for the analogue.* A searching algorithm for the best (closest to
 221 the target map) analogue among all the trajectory maps is implemented next.
 222 To increase the efficiency of this process, the search was done in two steps.

223 i. Optimization of the catalogue. First, selecting only “potential”
 224 analogues with a similar main drift reduces the Lagrangian
 225 catalogue. The trajectories centroid for each map of the catalogue
 226 is computed and compared to that of the target field, and finally
 227 discarding the analogues whose centroid was at a distance greater
 228 than δ_{cg} . The value of the δ_{cg} is selected to be small enough to
 229 minimize the computational time but sufficiently large to do not
 230 lose sampling variability in the potential analogues. We explored
 231 different values of this threshold distance to find that $\delta_{cg} = 2\xi = 10$
 232 km (where ξ is the spatial resolution) makes a good compromise
 233 between computational cost and number of potential analogues in
 234 both study areas.

235 ii. In a second step, we computed the Lagrangian errors (\mathcal{E}) between
 236 the trajectories of the target field and the potential analogues,
 237 defined as:

$$238 \quad \varepsilon_{ANL} = \sqrt{\frac{1}{T} \sum_{j=1}^T (\delta_{ANL}(t_i))^2}, \quad t_i = \{6, 12, 24, 36, 48 \text{ hours}\}, \quad (1)$$

239 where $T = 5$ is the number of elements of the set of times t_i , and
 240 $\delta_{ANL}(t_i)$ is the mean separation distance at time t_i between the
 241 trajectories belonging to the target field \mathbf{X}_T and each of the potential
 242 analogues \mathbf{X}_c , given by:

$$244 \quad \delta_{ANL}(t_i) = \frac{1}{N} \sum_{j=1}^N |X_T^j(t_i) - X_c^j(t_i)|, \quad (2)$$

245 being N the total number of trajectories j .

246 4. *Best analogue.* The selection of the best analogue is performed by the
 247 Equation (2), which is a simple measure of similarity between two datasets.
 248 The best analogue is selected as the element of the catalogue with the lowest
 249 \mathcal{E}_{ANL} . Figure 3 shows an example of the time series of \mathcal{E}_{ANL} values, through
 250 the catalogue of potential analogues for a specific case. Then we locate the
 251 time t_{ANL} corresponding to best analogue: $t_{ANL} \rightarrow \min(\mathcal{E}_{ANL}) = \mathcal{E}_{ANL}(t_{ANL})$:
 252 $\mathbf{X}_c(t_{ANL})$.

253 5. *Currents Prediction.* Once we have identified t_{ANL} , the short term forecast of
 254 the HFR velocity fields is given by the hourly velocity fields corresponding
 255 to the next 48 hours since t_{ANL} (hereinafter “L-STP fields”):

$$256 \quad \mathbf{X}_{STP}(t_c+1:t_c+48h) = \mathbf{X}_c(t_{ANL}+1:t_{ANL}+48h) \rightarrow \mathbf{V}_{STP}(t_f+1:t_f+48h) = \mathbf{V}_c(t_{ANL}+1:t_{ANL}+$$

 257 48h),

258

259 where $\mathbf{V}_C(t_{ANL})$ is the velocity field corresponding to the best analogue and
 260 \mathbf{V}_{STP} are the forecast currents.

261 Figure 2 provides an example of the selected analogue (Figure 2b) and
 262 corresponding L-STP fields (Figure 2d) for a given target field (Figure 2a) and the
 263 ‘truth’ trajectories for the following 48 hours from the date of the target field
 264 (Figure 2c). The associated temporal series of errors for the target field and the
 265 potential analogues are shown in Figure 3, where the value of ϵ_{ANL} is marked using
 266 a red dot (corresponding to the error between the trajectories of the L-STP field in
 267 Figure 2d and the truth trajectories for the forecast period in –Figure 2c).

268 To assess the performance of the methodology, we computed forecasted
 269 trajectories based on persistence of currents (hereinafter ‘persistence fields’ \mathbf{X}_{PRS}).
 270 To obtain simulated trajectories using persistence currents, the particles are
 271 advected during 48 hours using a constant (frozen) velocity field (given by the
 272 current velocity field, or target field, $\mathbf{V}(t_f)$) during the 48 hours of simulation:
 273 $\mathbf{V}(x,y,t_f+T) = \mathbf{V}(x,y,t_f)$, where t_f = current time and $T = \{1 : 48h\}$.

274 The mean drift of the truth forecasted trajectories, \mathbf{X}_{TRU} , is also computed for each
 275 simulation period (the mean drift is computed averaging over all the particle
 276 trajectory length during 48 hours).

277 The Lagrangian errors between the truth trajectories \mathbf{X}_{TRU} and the L-STP
 278 trajectories \mathbf{X}_{STP} were also computed as:

$$279 \quad \epsilon_{STP} = \sqrt{\frac{1}{T} \sum_{j=1}^T (\delta_{STP}(t_i))^2} = \sqrt{\frac{1}{T} \sum_{j=1}^T \left(\frac{1}{N} \sum_{j=1}^N \left(X_{TRU}^j(t_i) - X_{STP}^j(t_i) \right) \right)^2}, \quad (3)$$

280 where δ_{STP} is the mean separation distance between truth and the L-STP
 281 trajectories for $t = t : t+48$ (following 48 hours from the study time). To compare
 282 with persistence, we also compute the Lagrangian error between the truth
 283 trajectories \mathbf{X}_{TRU} and the trajectories derived from the persistence field \mathbf{X}_{PRS} ,

$$284 \quad \epsilon_{PRS} = \sqrt{\frac{1}{T} \sum_{j=1}^T (\delta_{PRS}(t_i))^2} = \sqrt{\frac{1}{T} \sum_{j=1}^T \left(\frac{1}{N} \sum_{j=1}^N \left(X_{TRU}^j(t_i) - X_{PRS}^j(t_i) \right) \right)^2}, \quad (4)$$

285 where δ_{PRS} is the mean separation distance between truth maps of trajectories,
 286 \mathbf{X}_{TRU} , and maps of trajectories from persistent velocity fields, \mathbf{X}_{PRS} , for $t = t:t+48$
 287 (following 48 hours from the study time)

288 All the process for the selection and validation of the analogue with the different
289 variables has been summarized in Figure 4. The time series and spatial distribution
290 of the ε_{STP} and ε_{PRS} errors have been analyzed for both study areas. Finally, ε_{STP}
291 and ε_{PRS} time series have also been calculated and compared to the time series of
292 the ε_{ANL} , in order to evaluate if the ε_{ANL} can be used as an indicator of the expected
293 skill of the L-STP with respect to the persistence.

294 Some parameters in the algorithm have to be tuned in order to optimize the results
295 and the computational cost. For instance, we found that the optimal number of
296 particle trajectories, N is equal to 25. All the trajectories have been computed
297 considering infinitesimal and passive particles without adding a diffusion term. To
298 this end we used the Lagrangian module included in the HFR_Progs MATLAB
299 package.

300 The ability of this method relies on the precision in finding two matching HFR
301 currents states over the entire region, which is dependant on the historical record of
302 observations used to build the catalogue and the dynamical representativity of the
303 catalogue. In this study we use four-year dataset (2012-2015) of trajectory maps
304 computed for the SE BoB, where the trajectory maps from the three first years
305 (2012-2014) were used as Lagrangian catalogue, and the remaining year (2015)
306 was used as a test period. The historical Lagrangian catalogue for this HFR system
307 is, thus, composed of 26304 maps of $N=25$ trajectories of 48-hours. Then the
308 method was applied to the Red Sea dataset, for the period of July 2017-October
309 2018. As the dataset temporal extension was short (1 year and 4 months), we have
310 used the whole period to build the Lagrangian catalogue and act as a test period at
311 the same time. In this case, for the analogues search the 5-days period around the
312 date of the target field was removed from the catalogue at each iteration, to avoid
313 temporal overlapping with the target field.

314

315 3. RESULTS

316 Figure 2 shows an example of the developed methodology applied to the BoB HFR
317 system on April 15, 2015. It is a visual representation of the (a) target trajectories,
318 (b) the selected analogue, (c) truth trajectories during the next 48 hours from the
319 target period, and (d) the L-STP trajectories provided by the method (48 hours
320 from the analogue).

321 The performance assessment results are described in section 3.1 and the temporal
322 and spatial forecast for both study areas are shown in section 3.2.

324 Figure 5 shows the ϵ_{ANL} through 2015 for the BOB study area, together with the
 325 ϵ_{STP} and ϵ_{PRS} . The analysis of this plot aims to check the relation between ϵ_{ANL} , ϵ_{STP}
 326 and ϵ_{PRS} . Black dots over the timeline in Figure 5 show the times when ϵ_{STP} is
 327 higher than the ϵ_{PRS} , which occurs 12% of the time. The mean value of the ϵ_{PRS} is
 328 73% higher than the ϵ_{STP} . The correlation between ϵ_{ANL} and ϵ_{STP} is 0.46 while
 329 correlation between ϵ_{ANL} and ϵ_{PRS} is 0.05, for the whole test year (2015). Focusing
 330 on the times when the ϵ_{PRS} is lower than the ϵ_{STP} , it can be seen that they mostly
 331 occur during winter months. Previous works in this area have shown that there are
 332 high persistent eastward currents that can last for several weeks during winter
 333 months (Solabarrieta et al., 2014), which can explain the better performance of the
 334 persistence fields in this period.

335 The hourly values of ϵ_{STP} and ϵ_{PRS} have been plotted against their corresponding
 336 hourly ϵ_{ANL} values for the test year, ordered from minimum to maximum along the
 337 x-axis in Figure 6. We observe that, when ϵ_{ANL} is low (less than 13.06 km for this
 338 data set), ϵ_{STP} is smaller than ϵ_{PRS} . However, as ϵ_{ANL} increases, ϵ_{STP} and ϵ_{PRS}
 339 converge until an inflection point beyond which ϵ_{STP} is slightly greater than ϵ_{PRS} .
 340 For the SE BoB experiment, the inflection point occurs at $\epsilon_{ANL} = 13.06$ km and 88%
 341 of cumulative ϵ_{ANL} . Results from the Red Sea HFR system indicates a similar
 342 pattern (not shown), when the inflection point occurs at $\epsilon_{ANL} = 12.81$ km and at
 343 86.4% of cumulative ϵ_{ANL} .

344 Further analysis to elucidate the mean separation distances (δ_{STP} and δ_{PRS}) related
 345 to ϵ_{ANL} after 6, 12, 24, 36 and 48 hours are presented hereinafter. ϵ_{ANL} has been
 346 plotted together with the mean separation distances of the trajectories (δ_{STP} and
 347 δ_{PRS}), after 6, 12, 24, 36 and 48 hours for each target field (Figure 7). δ_{STP} is always
 348 higher than the δ_{PRS} for the 6 hours' simulation. But the values of δ_{STP} show lower
 349 values than δ_{PRS} for the lowest ϵ_{ANL} for the simulations at 12, 24, 36 and 48 hours.

350 The values of the correlation coefficient (R^2) between the ϵ_{ANL} and δ_{STP} and
 351 between ϵ_{ANL} and δ_{PRS} after 6, 12, 24, 36 and 48 hours are summarized in Table 2,
 352 in order to analyze the relations between the Analogue, the L-STP and the
 353 persistence. Values of R^2 for ϵ_{ANL} and δ_{PRS} are small (almost no correlation),
 354 varying between 0.01 and 0.11, while correlations between ϵ_{ANL} and δ_{STP} are
 355 higher, varying between 0.19 and 0.56, and showing higher correlation (>than
 356 0.37) after 12 hours of simulations. The behavior of the Red Sea HFR system
 357 figures (not shown) is similar to the BoB HFR system.

358 Figures 6 and 7 (and the same ones for the Red Sea system, not shown) show that
 359 while ϵ_{ANL} increases, ϵ_{STP} and δ_{STP} increase, but ϵ_{PRS} and δ_{PRS} decrease, showing an
 360 inflexion point (hereinafter $\epsilon_{ANL(*)}$). The $\epsilon_{ANL(*)}$ can be calculated just for the
 361 historical dataset but ϵ_{ANL} can also be calculated in real time and compared with
 362 $\epsilon_{ANL(*)}$. It gives a reference value for the forecast skills:

$$363 \quad \epsilon_{ANL} < \epsilon_{ANL(*)} \rightarrow \delta_{STP} < \delta_{PRS} \quad \rightarrow \text{Use L-STP}$$

$$364 \quad \epsilon_{ANL} > \epsilon_{ANL(*)} \rightarrow \delta_{STP} > \delta_{PRS} \quad \rightarrow \text{Use Persistence}$$

365 To assess the capabilities of the L-STP methodology, times when $\epsilon_{ANL} < \epsilon_{ANL(*)}$
 366 have been just analyzed from now on, as when $\epsilon_{ANL} > \epsilon_{ANL(*)}$ we recommend to
 367 use persistent currents as a short term forecast.

368 *3.2 Spatio-temporal performances of the L-STP methodology*

369 Mean separation distances between truth and forecasted trajectories after different
 370 periods of integration times have been computed for both systems just for $\epsilon_{ANL} <$
 371 $\epsilon_{ANL(*)}$ times (Figure 6), in order to evaluate the temporal forecast capabilities of the
 372 methodology. Separation distances computed for the whole test year 2015, are
 373 shown in Figure 8, for the BoB HFR observations.

374 The separation distances between the measured trajectories and predicted persistent
 375 and STP trajectories, have similar values during the first 6 hours (4km) of the
 376 forecast period, with slightly better results for persistent trajectories. But after 6
 377 hours, the separation distance for the forecast based on persistent currents increases
 378 faster than using L-STP. At 24 hours, the separation distance is 11 km for
 379 persistence forecasts and 8km for L-STP forecasts. The values are 12 and 18km,
 380 respectively, after 48 hours of simulation. The mean drift values of the truth
 381 trajectories show that the mean drift is similar to the L-STP separation distances,
 382 during the 48 hours.

383 Temporal mean separation distances between truth and forecasted trajectories for
 384 the Central Red Sea HFR System, computed for $\epsilon_{ANL} < \epsilon_{ANL(*)}$ are shown in Figure
 385 9. The separation distances for the STP forecasts are higher than those forecasts
 386 with persistent currents during the first 15 hours. After 15 hours, quality of
 387 forecasts reversed where STP produced better results than persistence.

388 Spatial distribution of the difference between δ_{PRS} and δ_{STP} at 6, 12, 24 and 48
 389 hours, for the BoB and the Red Sea study areas, are shown in Figure 10 and Figure
 390 11.

391 For the BoB HFR system, the differences are not appreciated during the first 6
 392 hours. However, after 12 hours of simulation, the advantage of the L-STP is clear
 393 in most of the study area, especially outside the continental shelf slope where
 394 persistent currents dominate the circulation. The separation values between δ_{PRS}
 395 and δ_{STP} increase up to 10km after 48hours of simulation.

396 For the Red Sea, the significant differences between STP and Persistence start after
 397 24 hours of simulation, and continue until 48 hours.

398

399 4. DISCUSSION

400 In this work, a new methodology to forecast ocean surface currents based on HFR
 401 observations has been described. The approach is based on the search of analogues
 402 in a trajectory (Lagrangian) space using a previously generated trajectory field
 403 catalogue. The temporal and spatial skills of the proposed L-STP methodology
 404 have been analyzed in the previous section.

405 The target Lagrangian trajectory maps have been compared with the previously
 406 generated trajectory catalogue to obtain ϵ_{ANL} , ϵ_{STP} , ϵ_{PRS} , δ_{STP} and δ_{PRS} for each
 407 analyzed time. For the BoB system (2015 period), the correlation between ϵ_{ANL} and
 408 ϵ_{PRS} is 0.05, showing no relation between them and similar values are obtained for
 409 ϵ_{ANL} and δ_{PRS} (0.01-0.11- from table 2). The correlation between ϵ_{ANL} and ϵ_{STP} is
 410 0.46 and it varies from 0.19 to 0.56 between ϵ_{ANL} and δ_{STP} . Although the
 411 correlation between ϵ_{ANL} (past) and δ_{STP} or ϵ_{STP} (future) are low, they suggest that
 412 there is a relation between the errors of the analogues and the errors of the L-STP.
 413 δ_{STP} is always higher than the δ_{PRS} for the 6 hours' simulation. Which means that
 414 for the first hour, it is better to use persistence.

415 The $\epsilon_{ANL(*)}$ can just be calculated for the historical dataset but ϵ_{ANL} can also be
 416 calculated and compared to the previously selected $\epsilon_{ANL(*)}$, in real time. It gives a
 417 reference value for the forecast skills and we suggest that ϵ_{ANL} can be considered as
 418 a real-time skill-score metric for the L-STP :

$$419 \quad \epsilon_{ANL} < \epsilon_{ANL(*)} \rightarrow \delta_{STP} < \delta_{PRS} \quad \rightarrow \quad \text{Use L-STP}$$

$$420 \quad \epsilon_{ANL} > \epsilon_{ANL(*)} \rightarrow \delta_{STP} > \delta_{PRS} \quad \rightarrow \quad \text{Use Persistence}$$

421 The election of the best value for $\epsilon_{ANL(*)}$ is the main sensitive step of the proposed
 422 methodology: the values of ϵ_{ANL} are different for each study area and no fixed

423 value can be given. Due to this, an exhaustive analysis of ϵ_{ANL} , δ_{STP} , δ_{PRS} of the
424 historical dataset is required to find the correct inflexion point and select a correct
425 $\epsilon_{ANL(*)}$, before the method can be applied to a new study area.

426 Once fixed $\epsilon_{ANL(*)}$, the skills of the proposed L-STP methodology have been tested
427 in figures 8 to 11. The values of the δ_{STP} , compared to previous works in the BoB
428 area showed that the L-STP produces accurate predictions, which demonstrates the
429 ability of the Lagrangian approach to capture key dynamical features needed to
430 accurately predict the proper dynamical conditions.

431 For the BoB HFR System, temporal δ_{STP} shows values of 3.5km, 5.5km and 8km,
432 after 6, 12, and 24 hours respectively. The δ_{STP} values are similar to the δ_{PRS} values
433 during the first 6 hours of simulation but δ_{STP} are lower after that, with 3km and
434 5.5km of difference between them, after 24 and 48 hours of simulation,
435 respectively (*Figure 8*). As stated in previous work, that the circulation over the
436 BoB area is dominated by a stable, persistent current field during winter
437 (Solabarrieta et al., 2014) which is reflected by these results where persistence has
438 good or even slightly better forecasting skill during the first 6 forecast hours than
439 the proposed methodology.

440 δ_{STP} values for the BoB HFR system are similar to the ones obtained by
441 Solabarrieta *et al.*, 2016, for the whole year but δ_{STP} are better for summer months,
442 for the same study area. They used the linear autoregressive model, described in
443 Frolov et al., 2012, to forecast HFR current fields and the errors using that
444 approach were 2.9 and 7.9 km after 6 and 24 hours. Although the results obtained
445 in this work improve only during certain periods the forecast presented in
446 Solabarrieta et al., 2016, the presented methodology has three advantages over the
447 previous method: it is easy to run in real time; it does not require a continuous
448 training period; and it is able to discriminate the times when the usage of the
449 persistence is applicable. On the negative side, it requires the generation of a
450 catalogue of past trajectories as the search space for analogues, but once it is ready,
451 it is easily increasable in real time, without extra pre-analysis; just adding new
452 trajectory fields to the previous catalogue.

453 The values of the δ_{STP} for the Red Sea HFR system follow a similar pattern to the
454 BoB results, with higher separation distances. This may be related to the limited
455 time span of the available dataset, as a better closest analogue may be found in a
456 longer dataset.

457 The spatial comparison of the δ_{STP} and δ_{PRS} for the BoB HFR system (Figure 10),
458 shows that the L-STP has better skills for the entire study area after 12 hours of
459 simulations. The skills of the L-STP with respect to the persistence increases with
460 time, showing up to 10km of improvement relative to persistence at 48 hours in
461 some parts of the study area. For the spatial distribution, after 12 hours, the
462 smallest differences between δ_{STP} and δ_{PRS} occurred over the slope. This is
463 explained by the existence of persistent seasonal Iberian Poleward Current that
464 flows along the continental slope toward the east along the Spanish coast and
465 northward along the French coast (Solabarrieta *et al.*, 2014). In other words:
466 although the L-STP can be performant in periods of persistent currents, the
467 persistence field can show a better forecast for a short temporal scale (48h). L-STP
468 will improve those forecasts, as soon as spatio-temporal variability increases.

469 The results for the Red Sea HFR system are similar but the benefit of the L-STP
470 methodology appears only after 12 hours of simulation. Spatially, the improvement
471 is again lower where persistent currents occur, as it is the case of the Eastern
472 Boundary Current that flows northward following the eastern Red Sea Coastline in
473 the study area (Bower and Farrah, 2015; Sofianos and Johns, 2003; Zarokanellos *et*
474 *al.*, 2017b). The dominance of the persistent currents is evident in the lower values
475 of the difference between the STP forecasts and the Persistence forecasts as shown
476 in Figure 11 and in comparison, with Figure 10.

477 We have compared the capabilities of the L-STP methodology against the forecast
478 based on the persistence of currents. The L-STP method requires long (but not
479 continuous) training periods and improves the results obtained from previously
480 developed HFR forecast system (Solabarrieta *et al.*, 2016) in the same study area
481 (BoB) for the whole year. However, the L-STP still shows some limitations in
482 predicting some specific dynamical scenarios, i.e. the dynamical conditions
483 originated by the persistent IPC (Iberian Poleward Current). We have found that
484 the Lagrangian analogue is not able to properly identify such persistence, it
485 performs relatively better during non-persistent periods. The fact that persistent
486 events in both study areas are characterized by narrow high-speed jets (i.e. IPC in
487 the BoB) small spatial differences in the location of the main circulation could
488 generate high separation distances between the reference and predicted trajectories.
489 While the trajectory computed from the velocity field predicted from the
490 persistence model is advected in the same jet, the currents obtained from the L-
491 STP are slightly shifted, but just enough to advect the particle in a different
492 position within the jet, originating, therefore larger errors (larger ϵ_{STP}). We have
493 observed that the longer the training period (as in the BoB system), the better the
494 performance of the L-STP method. This suggests that longer training periods

495 would increasing the capability to identify periods of persistent dynamics
496 occurring over the same area, and thus improving the performance of the L-STP.

497 As mentioned, previous efforts to forecast surface currents from HFR data have
498 shown similar results compared with the methodology presented in this paper.
499 However, the advantage of the L-STP method is that it can be used in near-real
500 time, with short and non-continuous datasets of around 2-3 years.

501

502 5. CONCLUSION

503 A methodology forecast surface currents with analogues of Lagrangian dynamics
504 in real-time has been proposed. This methodology provides accurate forecast of sea
505 surface currents up to 48 hours and its capability has been tested in terms of spatial
506 and temporal distributions. The methodology has been successfully applied to two
507 distinct coastal regions to evaluate its capabilities in different hydrodynamic
508 regimes, although further analysis using data from more areas is required to
509 generalize the methodology.

510 Relationships between ϵ_{ANL} and $\epsilon_{STP}/\epsilon_{PRS}$ suggest that the ϵ_{ANL} can be considered
511 as a reliable indicator of the method's performance. Taking in consideration all the
512 analyses done in this work, we propose to use STP currents for trajectory or
513 velocity field predictions from 12 hours forward, if the ϵ_{ANL} value is lower than
514 $\epsilon_{ANL(*)}$. If ϵ_{ANL} is higher than $\epsilon_{ANL(*)}$, or the forecast is just for the next 6 hours, the
515 use of the persistence field is suggested. We also suggest that the $\epsilon_{ANL(*)}$ value and
516 forecast transition time need to be carefully evaluated for each study region. This,
517 of course, infers that a minimum data set is required before the L-STP method can
518 be applied.

519 Further analysis of analogue finding approaches is required to improve the
520 observed results, especially during periods when currents are persistent. The use of
521 longer dataset as a training period may improve this aspect. Then, the next step
522 would be to test the methodology for additional periods and other regions, to
523 analyze the possibility to find analogues for different sub-regions and to evaluate
524 its functionality in an operational mode.

525 The methods to find the minimum training period for each system should be
526 analyzed deeper in future works. The minimum training period will be directly
527 related to the variability of the local dynamics and those should be considered
528 during the analysis.

529 The HFR Progs MATLAB package ([https://](https://cencalarchive.org/~cocmpmb/COCMPwiki)
530 cencalarchive.org/~cocmpmb/COCMPwiki) has been used to generate total
531 currents from radial files and to fill the spatial gaps of the surface current field
532 using the OMA method, and to generate Lagrangian trajectories. The presented
533 forecasting method can be therefore easily implemented as an additional tool to
534 provide short term forecast at the same time that they generate total currents.

535 **DATA AVAILABILITY**

536 The Red Sea HF Radar data can be requested through:

- 537 ● <https://lthdatalib.kaust.edu.sa>

538 Historical and NRT Bay of Biscay HF Radar data can be requested through:

- 539 ● Euskoos portal: <https://www.euskoos.eus/en/data/basque-ocean-meteorological-network/high-frequency-coastal-radars/>

- 540 ● Emodnet Physics -

541 <http://www.emodnetphysics.eu/Map/platinfo/piradar.aspx?platformid=10273>

- 542 ● CMEMS Instac - http://marine.copernicus.eu/services-portfolio/access-to-products/?option=com_csw&view=details&product_id=INSITU_GLO_UV_NRT_OBSERVATIONS_013_048
- 543
- 544
- 545
- 546

547 **AUTHOR CONTRIBUTION**

- 548 ● **Lohitzune Solabarrieta:** She has worked on the set up of the methodology,
549 data analysis, manuscript writing and final submission.
- 550 ● **Ismael Hernandez-Carrasco:** He has worked on the set up of the
551 methodology and the manuscript writing.
- 552 ● **Anna Rubio:** She has worked on the set up of the methodology, data
553 analysis, and manuscript writing.
- 554 ● **Michael Campbell:** He has worked on the configuration of the
555 methodology. He has also contributed on the manuscript writing.
- 556 ● **Ganix Esnaola:** He has worked on the configuration of the methodology. He
557 has also contributed on the manuscript writing.
- 558 ● **Julien Mader:** He has contributed on the writing of the manuscript.
- 559 ● **Burton H. Jones:** He has contributed on the writing of the manuscript.
- 560 ● **Alejandro Orfila:** He has worked on the configuration of the methodology,
561 data analysis and the manuscript writing.

562 **COMPETING INTERESTS**

563 The authors declare that we have no conflict of interest

564 **ACKNOWLEDGEMENTS**

565 This work was funded by a Saudi Aramco-KAUST Center for Marine
566 Environmental Observation (SAKMEO) Postdoc fellowship to Lohitzune
567 Solabarrieta, and from the Integrated Ocean Processes (IOP) Group in KAUST.
568 We acknowledge the support of the LIFE-LEMA project (LIFE15
569 ENV/ES/000252), the European Union’s Horizon 2020 research and innovation
570 program under grant agreement No. 654410 & 871153 (JERICO-NEXT and
571 JERICO-S3 Projects), the Directorate of Emergency Attention and Meteorology of
572 the Basque Government, the MINECO/FEDER Project MOCCA (256RTI2018-
573 093941-B-C31). and the Department of Environment, Regional Planning,
574 Agriculture and Fisheries of the Basque Government (Marco Program). This work
575 was partially performed while A. Orfila was a visiting scientist at the Earth,
576 Environmental and Planetary Sciences Department at Brown University through a
577 Ministerio de Ciencia, Innovación y Universidades fellowship (PRX18/00218).
578 Ismael Hernandez-Carrasco acknowledges the Vicenç Mut contract funded by the
579 Balearic Island Govern and the European Social Fund (ESF) Operational
580 Programme. The HF radar-processing toolbox HFR_Progs use to produce OMA
581 was provided by D. Kaplan and M. Cook, Naval Postgraduate School, Monterey,
582 CA, USA.

583 **REFERENCES**

- 584 Abascal, A. J., Castanedo, S., Medina, R., Losada, I. J., Álvarez-Fanjul, E.:
585 Application of HF radar currents to oil spill modelling. *Mar. Pollut. Bull.* 58
586 (2), 238–248, 2009
- 587 Abascal A. J., Sanchez, J., Chiri, H., Ferrer, M. I., Cárdenas, M., Gallego, A.,
588 Castanedo, S., Medina, R., Alonso-Martirena, A., Berx, B., Turrell, W. R.,
589 Hughes, S. L.: Operational oil spill trajectory modelling using HF radar
590 currents: A northwest European continental shelf case study. *Marine*
591 *Pollution Bulletin*, Volume 119, Issue 1, Pages 336-350, ISSN 0025-326X,
592 <https://doi.org/10.1016/j.marpolbul.2017.04.010>, 2017.
- 593 Abualnaja, Y., Papadopoulos, V. P., Josey, S. A., Hoteit, I., Kontoyiannis, H., and
594 Raitzos, D. E.: Impacts of climate modes on air–sea heat exchange in the
595 Red Sea, *J. Clim.*, 28, 2665–2681, doi:10.1175/JCLI-D-14-00379.1, 2015.
- 596 Barrick, D. E.: Extraction of wave parameters from measured HF radar sea-echo
597 Doppler spectra. *Radio Sci.*, 12, 415–424, doi:10.1029/RS012i003p00415,
598 1977.
- 599 Barrick D.E., Fernandez, V., Ferrer, M.I., Whelan, C., and Breivik, Ø.: “A short-
600 term predictive system for surface currents from a rapidly deployed coastal
601 HF-Radar network,” *Ocean Dyn.*, vol. 62, no. 5, pp. 725–740, 2012.
- 602 Barth, A., Alvera-Azcárate, A., Beckers, JM., Staneva J., Stanev E.V., and [Schulz-](#)
603 [Stellenfleh](#) J.: Correcting surface winds by assimilating high-frequency
604 radar surface currents in the German Bight. *Ocean Dynamics*, 2011, vol 61:
605 599. <https://doi.org/10.1007/s10236-010-0369-0>, 2011.
- 606 Bellomo, L., Griffa, A., Cosoli, S., Falco, P., Gerin, R., Iermano, I., Kalampokis,
607 A., Kokkini, Z., Lana, A., Magaldi, M.G., Mamoutos, I., Mantovani, C.,
608 Marmain, J., Potiris, E., Sayol, J.M., Barbin, Y., Berta, M., Borghini, M.,
609 Bussani, A., Corgnati, L., Dagneaux, Q., Gaggelli, J., Guterman, P.,
610 Mallarino, D., Mazzoldi, A., Molcard, A., Orfila, A., Poulain, P. M.,
611 Quentin, C., Tintoré, J., Uttieri, M., Vetrano, A., Zambianchi, E. and
612 Zervakis, V.: Toward an integrated HF radar network in the Mediterranean
613 Sea to improve search and rescue and oil spill response: the TOSCA project
614 experience. Toward an integrated HF radar network in the Mediterranean
615 Sea to improve search and rescue and oil spill response: the TOSCA project

- 616 experience, *Journal of Operational Oceanography*, 8:2, 95-107, DOI:
617 10.1080/1755876X.2015.1087184, 2015.
- 618 Bower, A. S., and Farrar, J. T.: Air–sea interaction and horizontal circulation in the
619 Red Sea. In N. M. A. Rasul & I. C. F. Stewart, (Eds.), *The Red Sea*, Springer
620 Earth System Sciences (pp. 329–342). Berlin, Germany: Springer.
621 https://doi.org/10.1007/978-3-662-45201-1_19, 2015.
- 622 Breivik, Ø, and Saetra, Ø.: Real time assimilation of HF radar currents into a
623 coastal ocean model. *Journal of Marine Systems*, Volume 28, Issues 3–
624 4, April 2001, Pages 161-182. [https://doi.org/10.1016/S0924-
625 7963\(01\)00002-1](https://doi.org/10.1016/S0924-7963(01)00002-1), 2001.
- 626 Chao, Y., Li Z., Farrara, K., McWilliams, J.C., Bellingham, J., Capet, X., Chavez,
627 F., Choi, J., Davis, R., Doyle, J., Fratantoni, D. M., Li P., Marchesiello, P.,
628 Moline, M.A., Paduan, J., Ramp, S.: Development, implementation and
629 evaluation of a data-assimilative ocean forecasting system off the central
630 California coast. *Deep Sea Research*, Vol. 56, Issues 3-5, pp 100-126.
631 <https://doi.org/10.1016/j.dsr2.2008.08.011>, 2009.
- 632 Crombie, D. D.: Doppler Spectrum of Sea Echo at 13.56-Mc/s', *Nature* 175, 681-
633 682, 1955.
- 634 Declerck A., Delpy M., Rubio A., Ferrer L., Basurko O. C., Mader J. and Louzao
635 M. Transport of floating marine litter in the coastal area of the south-eastern
636 Bay of Biscay: A Lagrangian approach using modelling and
637 observations, *Journal of Operational Oceanography*, 12:sup2, S111-
638 S125, DOI: 10.1080/1755876X.2019.1611708, 2019.
- 639 Emery, B. M., Washburn L., and Harlan, J. A.: Evaluating radial current
640 measurements from CODAR high-frequency radars with moored current
641 meters. *J. Atmos. Oceanic Technol.*, 21, 1259–1271, doi:10.1175/1520-
642 0426(2004)021,1259: ERCMFC.2.0.CO;2, 2004.
- 643 Esnaola, G., Sáenz, J., Zorita, E., Fontán, A., Valencia, V., and Lazure, P.: Daily
644 scale wintertime sea surface temperature and IPC-Navidad variability in the
645 southern Bay of Biscay from 1981 to 2010, *Ocean Sci.*, 9, 655–679,
646 <https://doi.org/10.5194/os-9-655-2013>, 2013.

- 647 Frolov, S., Paduan J., Cook M., and Bellingham J.: Improved statistical prediction
648 of surface currents based on historic HF- radar observations. *Ocean Dyn.*,
649 62, 1111–1122, doi:10.1007/ s10236-012-0553-5, 2012.
- 650 Hammond, T.M., Pattiaratchi ,C.B., Osborne, M.J., Nash, L.A., Collins, M.B.:
651 Ocean surface current radar (OSCR) vector measurements on the inner
652 continental shelf. *Continental Shelf Research. Volume 7, Issue 4*, Pages
653 411-431. [https://doi.org/10.1016/0278-4343\(87\)90108-7](https://doi.org/10.1016/0278-4343(87)90108-7), 1987.
- 654 Hernández-Carrasco, I., López, C., Hernández-García, E. & Turiel, A. How
655 reliable are finite-size Lyapunov exponents for the assessment of ocean
656 dynamics? *Ocean Modelling* 36, 208–218, 2011.
- 657 Hernández-Carrasco, I., Solabarrieta, L., Rubio, A., Esnaola, G., Reyes, E., and
658 Orfila, A.: Impact of HF radar current gap-filling methodologies on the
659 Lagrangian assessment of coastal dynamics, *Ocean Sci.*, 14, 827-847,
660 <https://doi.org/10.5194/os-14-827-2018>, 2018.
- 661 Hernández-Carrasco, I., Orfila, A., Rossi, V., and Garçon, V.: Effect of small-scale
662 transport processes on phytoplankton distribution in coastal seas, *Scientific*
663 *Reports*, 8:8613, <https://doi.org/10.1038/s41598-018-26857-9>, 2018b.
- 664 Jianping H., Yuhong Y., Shaowu W and Jifen C.: An analogue-dynamical long-
665 range numerical weather prediction system incorporating historical
666 evolution. *Q. J. R. Meteorol. Soc.*, 119, pp.547-565, 1993.
- 667 Kaplan, D. M. and Lekien, F.: Spatial interpolation and filtering of surface current
668 data based on open-boundary modal analysis, *Journal of Geophysical*
669 *Research: Oceans*, 112, <https://doi.org/10.1029/2006JC003984>, c12007,
670 2007.
- 671 Kohut, J.T., Glenn, S.M.: Improving HF radar surface current measurements with
672 measured antenna beam patterns. *J. Atmos. Oceanic Technol.* 20 (9), 1303–
673 1316, 2003.
- 674 Lana, A., Marmain, J., Fernández, V., Tintoré, J., Orfila A.: Wind influence on
675 surface current variability in the Ibiza Channel from HF Radar. *Ocean*
676 *Dynamics*, 66: 483. <https://doi.org/10.1007/s10236-016-0929-z>, 2016.

- 677 Langodan S., Cavaleri L., Vishwanadhapalli Y., Pomaro A., Bertotti L., Hoteit I.:
678 Climatology of the Red Sea - Part 1: the wind. *Int. J. Climatol.* 37: 4509–
679 4517. DOI: 10.1002/joc.5103, 2017.
- 680 Liu Y., Weisberg, R.H., and Merz, C.R.: Assessment of CODAR SeaSonde and
681 WERA HF Radars in Mapping Surface Currents on the West Florida Shelf.
682 *Journal of atmospheric and oceanic technology*, Vol 31., pp 1363:1382,
683 2014.
- 684 Barrick D.E. and Lipa B.J. (1979) A Compact Transportable HF Radar System for
685 Directional Coastal Wave Field Measurements. In: Earle M.D., Malahoff A.
686 (eds) *Ocean Wave Climate. Marine Science*, vol 8. Springer, Boston, MA.
687 https://doi.org/10.1007/978-1-4684-3399-9_7, 1979.
- 688 Lorenz, E. N.: Atmospheric Predictability as Revealed by Naturally Occurring
689 Analogues. *Journal of Atmospheric Sciences*, Volume 29, pp 636-646, 1969.
- 690 Manso-Narvarte, I., Caballero, A., Rubio, A., Dufau, C., and Birol, F.: Joint
691 analysis of coastal altimetry and high-frequency (HF) radar data:
692 observability of seasonal and mesoscale ocean dynamics in the Bay of
693 Biscay, *Ocean Sci.*, 14, 1265–1281, [https://doi.org/10.5194/os-14-1265-](https://doi.org/10.5194/os-14-1265-2018)
694 2018, 2018.
- 695 Oke, P. R., Allen, J. S., Miller, R. N., Egbert, G. D., and Kosro P. M.: Assimilation
696 of surface velocity data into a primitive equation coastal ocean model, *J.*
697 *Geophys. Res.*, 107, 3122, doi:10.1029/2000JC000511, 2002.
- 698 Orfila A., Molcard, A., Sayol, J.M., Marmain, J., Bellomo, L., Quentin, C., and
699 Barbin, Y.: Empirical Forecasting of HF-Radar Velocity Using Genetic
700 Algorithms *IEEE Transactions on Geoscience and Remote Sensing*, Vol. 53,
701 No. 5, 2015.
- 702 Ohlmann, C., White, P., Washburn, L., Emery, B., Terrill, E., Otero, M.:
703 Interpretation of coastal HF radar-derived surface currents with high-
704 resolution drifter data. *J. Atmos. Oceanic Technol.* 24 (4), 666–680, 2007.
- 705 Paduan, J.D., and Rosenfeld, L.K.: Remotely sensed surface currents in Monterey
706 Bay from shore-based HF radar (coastal ocean dynamics application radar. *J.*
707 *Geophys. Res.* 101 (C9), 20669–20686, 1996.

- 708 Paduan, J.D., and Shulman, I.: HF radar data assimilation in the Monterey Bay
709 area. *J. Geophys Res.* 109:C07S09, 2004.
- 710 Paduan, J.D., Kim, K.C., Cook, M. S., and Chavez, F.P.: Calibration and
711 Validation of Direction-Finding High-Frequency Radar Ocean Surface
712 Current Observations. *IEEE Journal of oceanic engineering*, Vol. 31, No. 4,
713 2006.
- 714 Paduan, J.D., and Washburn, L.: High-Frequency Radar Observations of Ocean
715 Surface Currents. *Annual Rev. Marine. Sci.* 2013.5:115-136, 2013.
- 716 Prince, K., X. and Goswami, B., N.: An Analog Method for Real-Time Forecasting
717 of Summer Monsoon Subseasonal Variability. *Monthly weather review*, Vol
718 135, pp: 4149-4160. <https://doi.org/10.1175/2007MWR1854.1>, 2007.
- 719 Ren L., Miaro, J., Li Y., Luo, X., Li J. and Hartnett, M.: Estimation of Coastal
720 Currents Using a Soft Computing Method: A Case Study in Galway Bay,
721 Ireland. *Mar. Sci. Eng.*, 7(5), 157; <https://doi.org/10.3390/jmse7050157>,
722 2019.
- 723 Roarty, H., Cook, T., Hazard, L., George, D., Harlan, J., Cosoli, S., Wyatt, L.,
724 Alvarez Fanjul, E., Terrill, E., Otero, M., Largier, J., Glenn, S., Ebuchi, N.,
725 Whitehouse, B., Bartlett, K., Mader, J., Rubio, A., Corgnati, L., Mantovani,
726 C., Griffa, A., Reyes, E., Lorente, P., Flores-Vidal, X., Saavedra-Matta, K.J.,
727 Rogowski, P., Prukpitikul, S., Lee, S.H., Lai, J.W., Guerin, C.A., Sanchez,
728 J., Hansen, B. and Grilli, S.: The Global High Frequency Radar Network.
729 *Front. Mar. Sci.* 6:164. doi: 10.3389/fmars.2019.00164, 2019.
- 730 Rubio, A., Fontán A., Lazure P., González M., Valencia V., Ferrer L., Mader J.
731 and Hernández C., 2013a: Seasonal to tidal variability of currents and
732 temperature in waters of the continental slope, southeastern Bay of Biscay. *J.*
733 *Mar. Syst.*, **109–110** (Suppl.), S121–S133, doi:10.1016/j.jmarsys.2012.01.004.
- 734 Rubio, A., Solabarrieta L. , González M., Mader J., Castanedo S., Medina R., Charria
735 G. and Aranda J., 2013b: Surface circulation and Lagrangian transport in the
736 SE Bay of Biscay from HF radar data. *MTS/IEEE OCEANS—Bergen, 2013*,
737 IEEE, 7 pp., doi:10.1109/OCEANS-Bergen.2013.6608039
- 738 Rubio, A., Mader, J., Corgnati, L., Mantovani, C., Griffa, A., Novellino, A.,
739 Quentin, C., Wyatt, L., Schulz-Stellenfleth, J., Horstmann, J., Lorente, P.,
740 Zambianchi, E., Hartnett, M., Fernandes, C., Zervakis, V., Goringe, P.,

- 741 Melet, A., and Puillat, I.: HF radar activity in European coastal seas: next
742 steps towards a pan-European HF radar network, *Front. Mar. Sci.*, 4,
743 8, <https://doi.org/10.3389/fmars.2017.00008>, 2017.
- 744 Rubio, A., Caballero, A., Orfila, A., Hernández-Carrasco, I., Ferrer, L., González,
745 M., Solabarrieta, L., and Mader, J.: Eddy-induced cross-shelf export of high
746 Chl-a coastal waters in the SE Bay of Biscay, *Remote Sens. Environ.*, 205,
747 290–304, 2018.
- 748 Rubio, A., Manso-Narvarte, I., Caballero, A., Corgnati, L., Mantovani, C., Reyes,
749 E., et al. The seasonal intensification of the slope iberian poleward current.
750 copernicus marine service ocean state report. *J. Oper. Oceanogr.* 12, 13–18.
751 doi: 10.1080/1755876X.2019.1633075, 2019.
- 752 Rubio, A., Hernández-Carrasco, I., Orfila, A., González, M., Reyes, E., Corgnati,
753 L., et al. (2020). A lagrangian approach to monitor local particle retention
754 conditions in coastal areas. copernicus marine service ocean state report. *J.*
755 *Oper. Oceanogr.* 13:1785097, 2020.
- 756 Sayol, J.M., Orfila, A., Simarro, G., Conti, G., Renault, L., Molcard, A. A
757 Lagrangian model for tracking surface spills and SaR operations in the
758 ocean, *Env. Mod. & Software*, (52), 74-82, 2014.
759 doi:10.1016/j.envsoft.2013.10.013.
- 760 Schmidt, R.: Multiple emitter location and signal parameter estimation. *IEEE*
761 *Trans. Antennas Propag.*, 34, 276–280, doi:10.1109/TAP.1986.1143830,
762 1986.
- 763 Schott F., Frisch, A.S., Leaman, K., Samuels, G., Popa Fotino, I.: High-Frequency
764 Doppler Radar Measurements of the Florida Current in Summer 1983. *J.*
765 *Geo. Research*, Vol 90, No C5, pp 9006:9016, 1985.
- 766 Shao, Q. and Li, M.: An improved statistical analogue downscaling procedure for
767 seasonal precipitation forecast . *Stoch Environ Res Risk Assess* 27, pp.: 819-
768 830. <https://doi.org/10.1007/s00477-012-0610-0>, 2013.
- 769 Sofianos, S. S., and Johns, W. E.: An oceanic general circulation model (OGCM)
770 investigation of the Red Sea circulation: 2. Three- dimensional circulation in
771 the Red Sea. *Journal of Geophysical Research*, 108(C3), 3066.
772 <https://doi.org/10.1029/2001jc001185>, 2003.

- 773 Solabarrieta, L., Rubio, A., Castanedo, S., Medina, R., Charria, G., Hernández, C.:
774 Surface water circulation patterns in the southeastern Bay of Biscay: new
775 evidences from HF radar data. *Cont Shelf Res* 74:60–76
776 doi:10.1016/j.csr.2013.11.022, 2014.
- 777 Solabarrieta, L., Rubio, A., Cárdenas, M., Castanedo, S., Esnaola, G., Méndez,
778 F.J., Medina, R., and Ferrer, L.: Probabilistic relationships between wind
779 and surface water circulation patterns in the SE Bay of Biscay. *Ocean Dyn.*,
780 65, 1289–1303, doi:10.1007/s10236-015-0871-5, 2015.
- 781 Solabarrieta, L., Frolov, S., Cook, M., Paduan, J., Rubio, A., González, M., Mader,
782 J., and Charria, G.: Skill Assessment of HF Radar–Derived Products for
783 Lagrangian Simulations in the Bay of Biscay. *J. Atmos. Oceanic Technol.*,
784 33, 2585–2597, doi: 10.1175/JTECH-D-16-0045.1, 2016.
- 785 Stanev, E.V., Schulz-Stellenfleth, J., Staneva, J., Grayek, S., Seemann, J. and
786 Petersen, W.: Coastal observing and forecasting system for the German
787 Bight – estimates of hydrophysical states. *Ocean Sci.*, 7, 569–583, 2011^[L]_[SEP]
788 doi:10.5194/os-7-569-2011, 2011.
- 789 Ullman, D.S., O'Donnell, J., Kohut, J., Fake, T., Allen, A.: Trajectory prediction
790 using HF radar surface currents: Monte Carlo simulations of prediction
791 uncertainties. *J. Geophys. Res.* 111 (C12005), 1–14, 2006.
- 792 Vilibić, I., Šepić, J., Mihanović, H., Kalinić, H., Cosoli, S., Janeković, I., Žagar,
793 N., Jesenko, B., Tudor, M., Dadić, V. and Ivanković, D.: Self-organizing
794 maps-based ocean currents forecasting system. *Scientific Reports* 6, 22924,
795 2016.
- 796 Yao, F., Hoteit, I., Pratt, L. J., Bower, A. S., Zhai, P., Kohl, A., and
797 Gopalakrishnan, G.: Seasonal overturning circulation in the Red Sea: 1.
798 Model validation and summer circulation, *J. Geophys. Res. Oceans*, 119,
799 doi:10.1002/2013JC009004, 2014a.
- 800 Yao, F., Hoteit, I., Pratt, L. J., Bower, A. S., Kohl, A., Gopalakrishnan, G., and
801 Rivas, D.: Seasonal overturning circulation in the Red Sea: 2. Winter
802 circulation, *J. Geophys. Res. Oceans*, 119, 2263–2289, doi:10.1002/
803 2013JC009331, 2014b.
- 804 Zarokanellos, N. D., Kürten, B., Churchill, J. H., Roder, C., Voolstra, C. R.,
805 Abualnaja, Y., and Jones, B. H.: Physical mechanisms routing nutrients in

- 806 the central Red Sea. *Journal of Geophysical Research: Oceans*, 122.
807 <https://doi.org/10.1002/2017JC013017>, 2017a.
- 808 Zarokanellos, N. D., Papadopoulos, V. P., Sofianos, S. S., and Jones, B. H.:
809 Physical and biological characteristics of the winter-summer transition in the
810 Central Red Sea. *Journal of Geophysical Research: Oceans*, 122, 6355–
811 6370. <https://doi.org/10.1002/2017JC012882>, 2017b.
- 812 Zhan, P., Subramanian, A. C., Yao, F., and Hoteit, I.: Eddies in the Red Sea: A
813 statistical and dynamical study, *J. Geophys. Res. Oceans*, 119, 3909–3925,
814 doi:10.1002/2013JC009563, 2014.
- 815 Zelenke B. C.: An Empirical Statistical Model Relating Winds and Ocean Surface
816 Currents. Master of Science in Oceanography - Thesis, Oregon State
817 University, 2005.

818 **TABLES**819 *Table 1: Characteristics of the previously developed STP works based on HFR data.*

Authors	Approach	Needs continuous training period	Complementary data required?	Region of application	Reliable forecast period
Zelenke 2005	EOF + bilinear regression model	Yes	Wind	Oregon coast	48 hours
Frolov et al. 2012	EOF + linear auto regression model	Yes	Wind and tides (optional)	Monterey Bay, California	48 hours
Barrick et al., 2012	Constant linear trend model applied to OMA modes	Yes	Wind	Finnmark, Norway	12 hours
Orfila et al. 2015	EOF+Genetic Algorithm	Yes	No	Toulon, France	48 hours
Solabarrieta et al. 2016	Frolov et al., 2012	Yes	No	Bay of Biscay	48 hours
Vilibić et al., 2016	SOM+neural network +winds	Yes	Wind	Northern Adriatic Sea	72 h
Ren et al., 2019	Random Forest (RF) classification algorithm	No	Tide and Wind	Galway Bay, Ireland	59 h
This paper: L-STP	Analogue finding	No	No	Bay of Biscay and the Central Red Sea	48 h

820

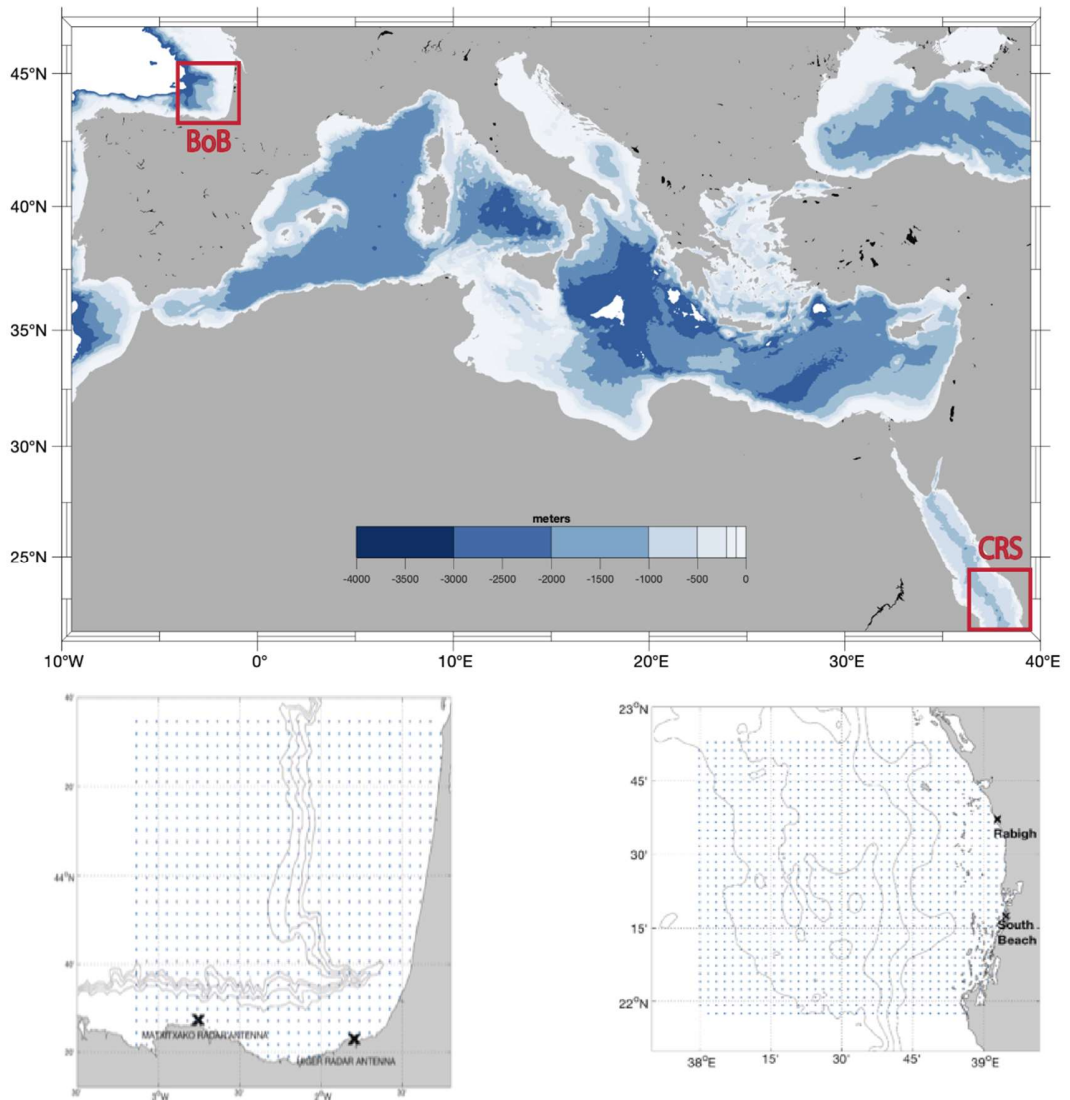
821 *Table 2: Correlation coefficient values between best ϵ_{ANL} and δ_{STP} and between ϵ_{ANL} and*
 822 *δ_{PRS} , after 6, 12, 24, 36 and 48 hours of simulation.*

	6 hours	12 hours	24 hours	36 hours	48 hours
$R^2 \epsilon_{ANL} - \delta_{STP}$	0.19	0.37	0.55	0.56	0.54
$R^2 \epsilon_{ANL} - \delta_{PRS}$	0.07	0.11	0.03	0.01	0.04
ϵ_{ANL} [km], for the inflection point between δ_{STP} and δ_{PRS}	-	11.94	12.44	13.09	14.33
% of ϵ_{ANL} (accumulative) for the previous line	-	81	84	87	95

823

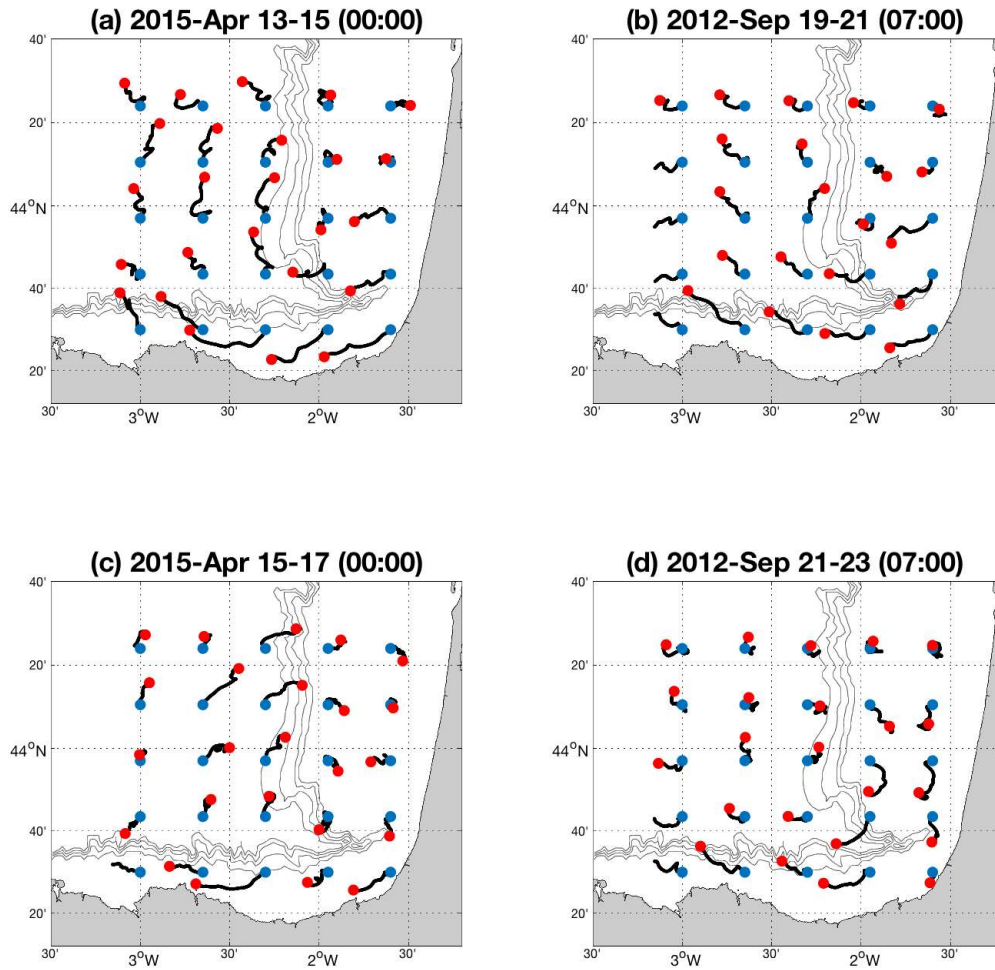
824 **FIGURES**

825 *Figure 1: (Up) A global view of both analyzed study areas. (Down-Left) HFR*
826 *system of the BoB. (Down-Right) HFR system of the central Red Sea. Blue dots*
827 *represent the data points and the black cross are the HFR antenna positions*



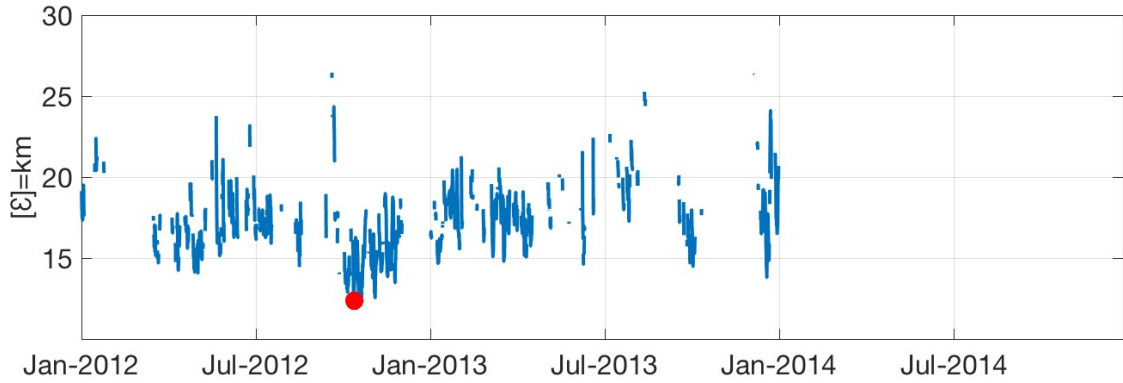
828

829 *Figure 2: (1) 15-Apr-2015 00:00 example of the developed methodology applied to*
 830 *the BoB HFR system. (a) The past 48 hours of target field of test period (b) The*
 831 *analogue having the lowest error, (c) The truth trajectories for the forecast period*
 832 *(d) the STP trajectories. The initial positions of the particle trajectories are*
 833 *indicated by the blue dots, and the red dots indicate the position after 48 hours.*



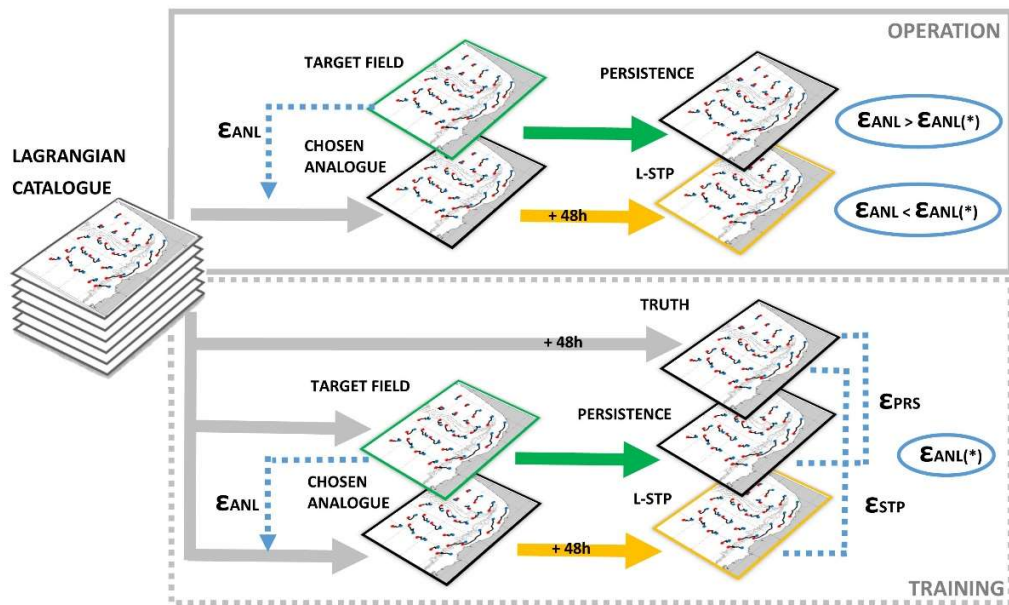
834

835 *Figure 3: Example for the test period on 15-Apr-2015 00:00; errors for the whole*
836 *Lagrangian catalogue fields of the BoB HFR System (training period 2012-2014),*
837 *restricted to the $\delta_{cg} = 10$ km condition. The red dot indicates the occurrence date*
838 *and the error of the best analogue (19-Sep-2012 07:00).*



839

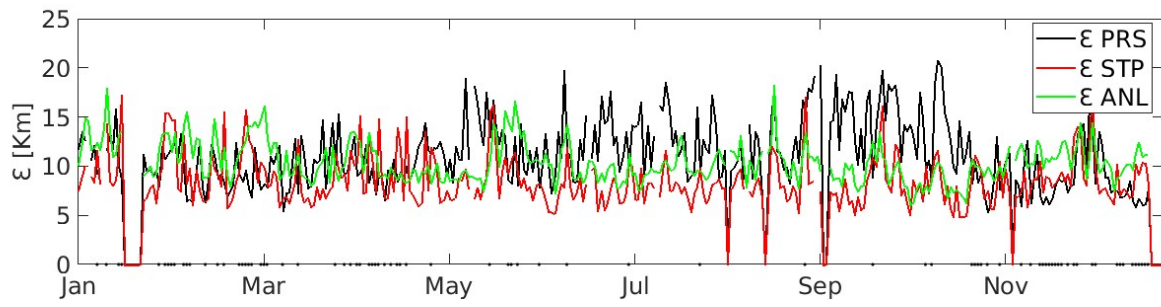
840 *Figure 4: Scheme of the analogue selection and L-STP forecast assessment*
 841 *process.*



842

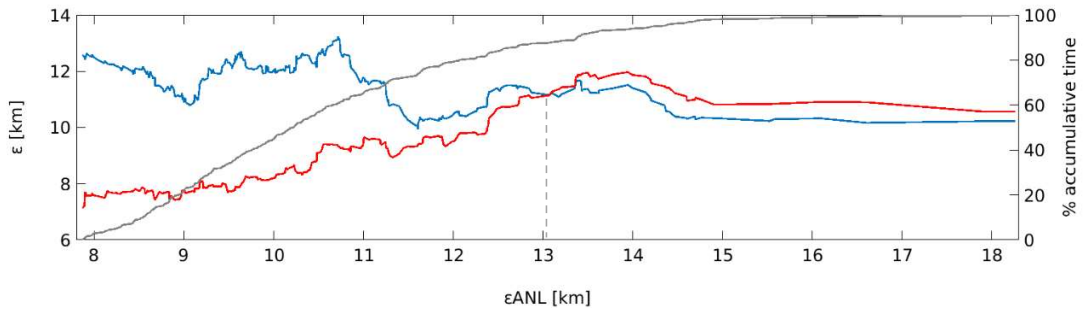
843

844 *Figure 5: errors of the hourly best analogue for the BoB HFR, for 2015 (ϵ_{ANL}),*
845 *together with the ϵ_{STP} and ϵ_{PRS} . The black dots over the timeline show the times*
846 *when ϵ_{STP} is higher than ϵ_{PRS}*



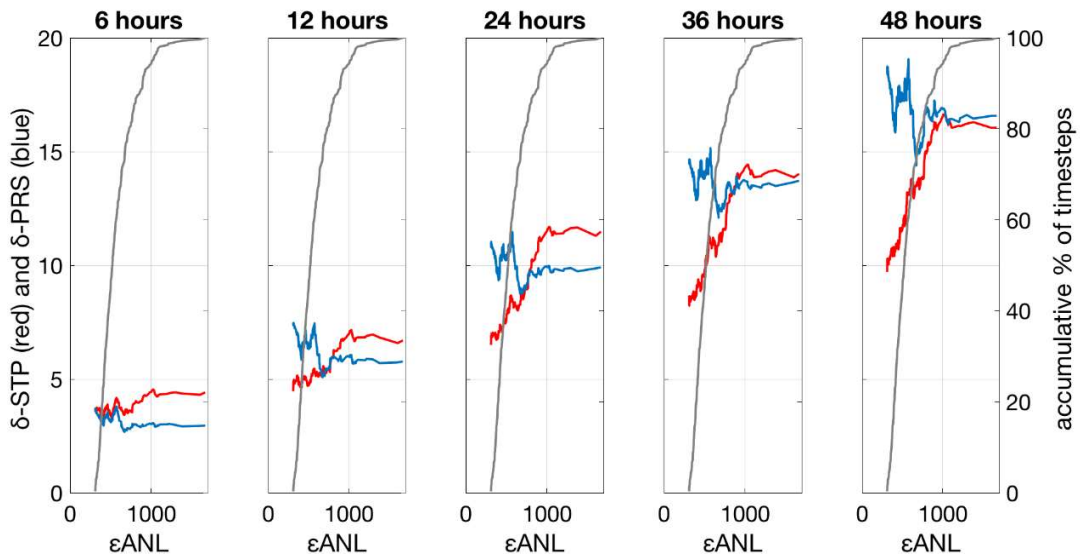
847

848 *Figure 6: X axis shows the ϵ_{ANL} , ordered from minimum to maximum, for the best*
 849 *analogue for the test year 2015, for the BoB HFR. Left Y axis indicates ϵ_{STP} (red)*
 850 *and ϵ_{PRS} (blue) for the corresponding ϵ_{ANL} . Right Y axis indicates the % of the*
 851 *accumulative comparison times as shown by the gray solid line. Dashed vertical*
 852 *line indicates the crossing point between ϵ_{STP} and ϵ_{PRS} ($\epsilon_{ANL}^*=13.06$ km).*



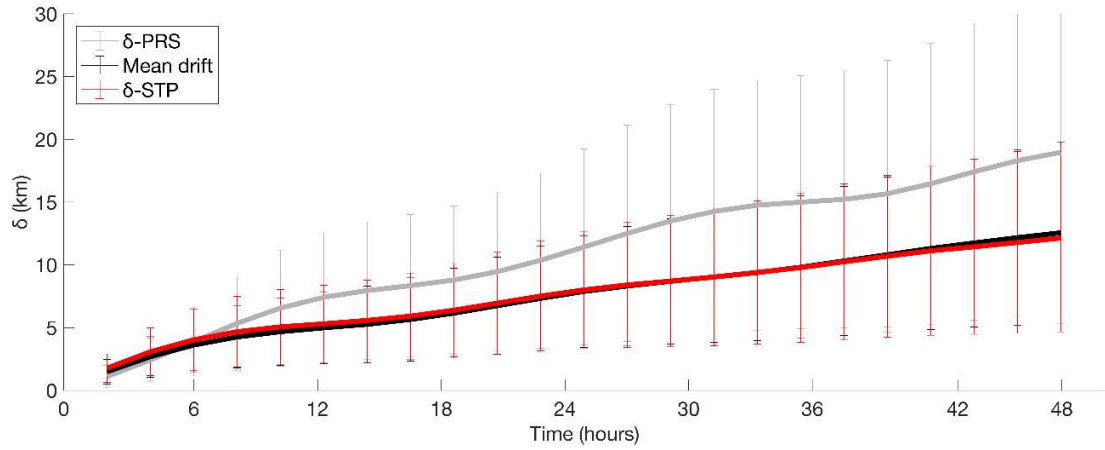
853

854 *Figure 7: Left Y axis indicates δ_{STP} (red) and δ_{PRS} (blue) for the corresponding*
 855 *ϵ_{ANL} , after 6, 12, 24, 36 and 48 hours. Right Y axis is the cumulative % of timesteps*
 856 *in the computation of the mean errors, as indicated by the black line in the plots. X*
 857 *axis is the ϵ_{ANL} , ordered from minimum to maximum, for the best analogue for the*
 858 *test year 2015 (BoB HFR system)*



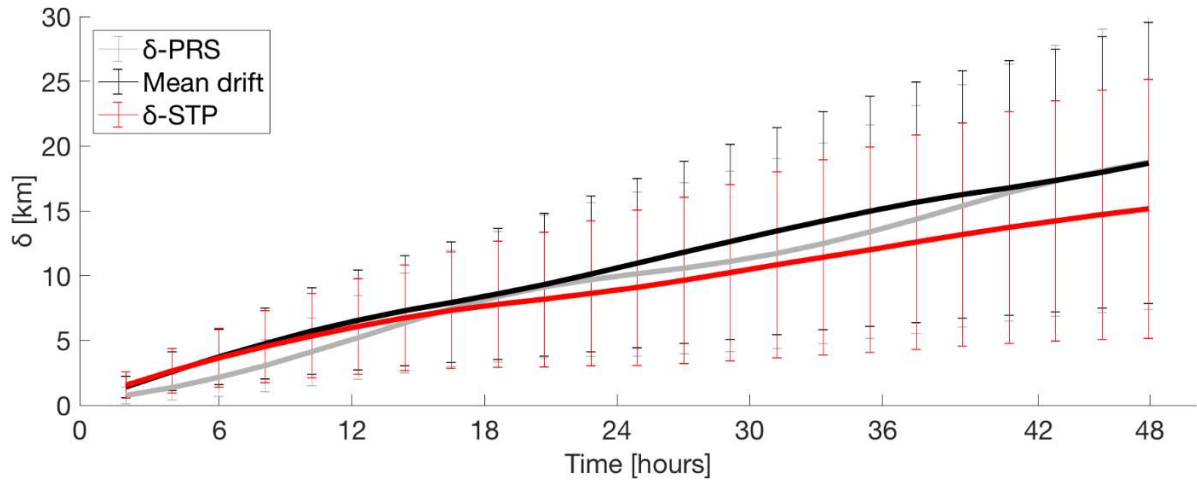
859

860 *Figure 8: Time evolution of the mean separation δ_{STP} and δ_{PRS} [km] between*
861 *truth and forecast trajectories using truth and STP/PRS currents and the mean*
862 *drift, with BoB system data, for 2015. The mean drift of the truth forecasted*
863 *trajectories is also computed for each simulation period (the means drift is*
864 *considered as the average of the distances moved by each particle during 48*
865 *hours).*



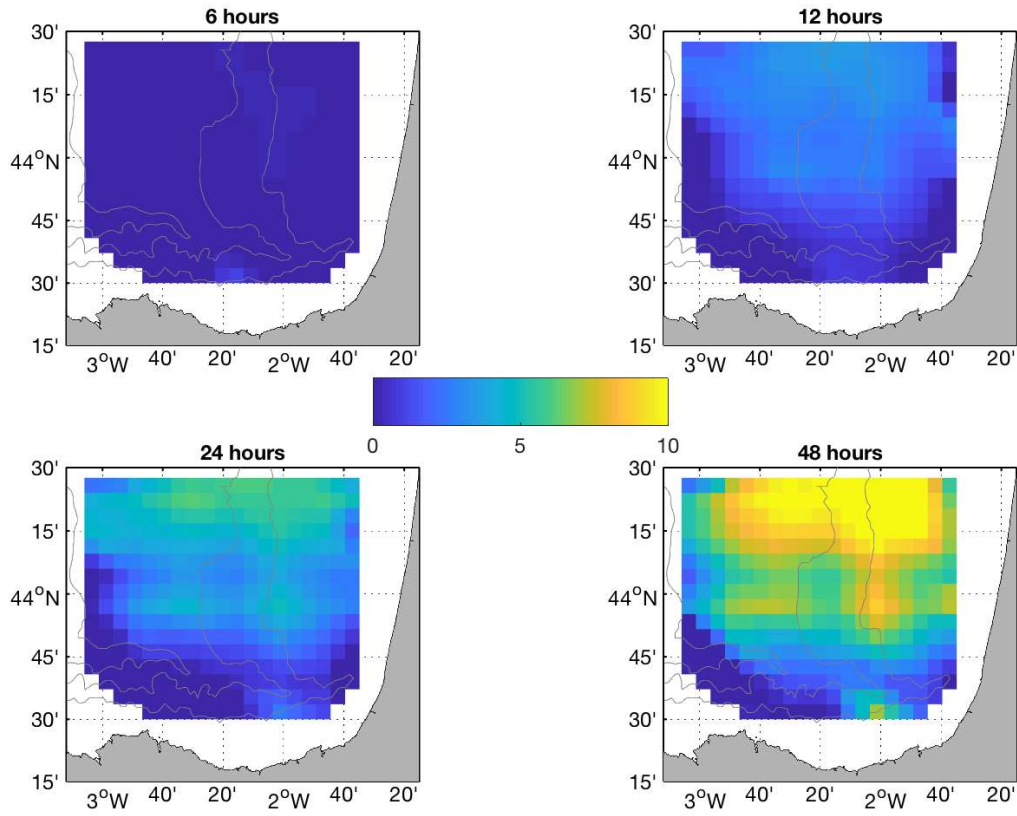
866

867 *Figure 9: Time evolution of the mean separation distances δ_{STP} and δ_{PRS} [km]*
868 *between real and forecast trajectories using truth and STP/PRS currents and the*
869 *mean drift, with the Red Sea HFR system data, for July 2017 to October 2018. The*
870 *mean drift of the truth forecasted trajectories is also computed for each simulation*
871 *period (the means drift is considered as the average of the distances moved by*
872 *each particle during 48 hours).*



873

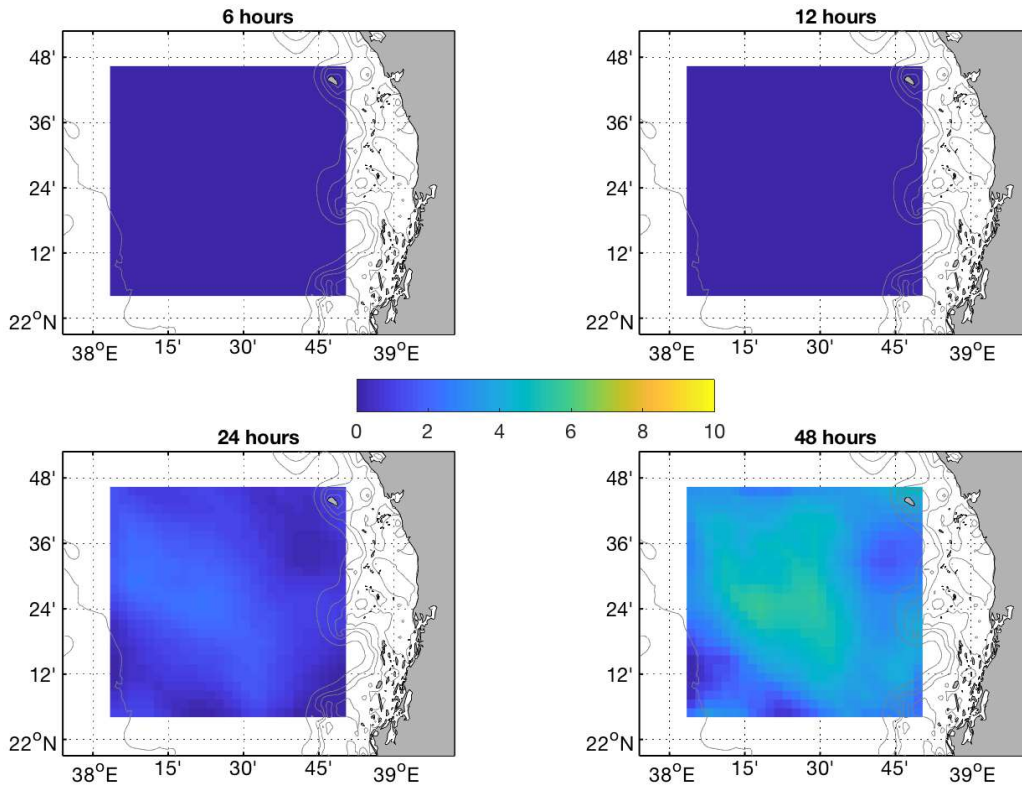
874 *Figure 10: Spatial distribution of separation distances [km] between trajectories*
875 *using L-STP and persistent currents at 6, 12, 24 and 48 hours, for the BoB HFR*
876 *System.*



877

878 *Figure 11: Spatial distribution of separation distances [km] between trajectories*
879 *using L-STP and persistent currents at 6, 12, 24 and 48 hours, for the Red Sea*
880 *HFR system.*

881



882